Volumetric laser heating of nanosuspension microdroplets: Slow evaporation to mid-air explosion

Tianyi Li[a], Aravinda Kar[b], Ranganathan Kumar[a],*

[a] Department of Mechanical and Aerospace Engineering, University of Central Florida, Orlando, Florida, 32816, USA
[b] CREOL, The College of Optics and Photonics, University of Central Florida, Orlando, Florida, 32816, USA

ARTICLE INFO

ABSTRACT

Opto-thermal interaction between a laser beam and a nanosuspension droplet is studied in this paper to analyze the thermal response of the droplet at different laser intensities depending on the optical properties of the nanosuspensions. A pulsed Nd:YAG laser beam is used to irradiate four types of droplet, 20 wt% silver nanoparticle suspension, 10 wt% and 5 wt% germanium nanoparticle suspension and 8 mM SDS solution, in an electrospray laser deposition experiment to observe the geometrical changes in their shape. A high-speed camera captured the images of the droplets, showing the decrease in their diameter and inception time for droplet slow evaporation as well as the pre-explosion time and an explosion regime map of four different explosion patterns: shallow, deep, directional and isotropic explosions depending on the laser peak intensity for 20 wt% silver nanoparticle suspension microdroplet. The other three types of suspension, however, do not undergo slow evaporation or experience mid-air explosion. A theoretical conduction model has been developed to predict the explosion of the droplet by finding its bubble formation region inside the droplet. These results are corroborated by experiments that the explosion characteristics depend on the optical properties of the suspension such as reflectance, absorption coefficient and refractive index. The temperature distribution and the predicted bubble formation region for the four types of suspension are investigated, and only the silver nanoparticle suspension of 20 wt% with low reflectance and high absorption coefficient is predicted to have bubble formation patterns within the droplet, similar to the four explosion patterns in the experiment. The conduction model agrees well with the experimental results and shows that it can predict the threshold laser peak intensity and explosion patterns of a droplet a priori at which explosion occurs.

© 2021 Elsevier Ltd. All rights reserved.

1. Introduction

Printing nanopatterns additively on substrates is of importance in nanophotonic and optoelectronic devices [1]. These nanostructure patterns have better mechanical and optical properties as well as lower melting temperature compared to the bulk material [2], and can be deposited on the substrate by using the nano-electrospray laser deposition method or printing and laser curing [1,3]. Water droplets in the range of 60–100 μm containing semiconductor nanoparticles are ejected from an electrospray in the microdripping mode [4]. A focused Nd:Yag laser beam evaporates the water while simultaneously sintering the nanoparticles on the substrate [2,5]. Laser sintering has also been used in manufacturing organic field-effect transistors due to its high resolution and low cost [6,7].

An important aspect of laser heating is to understand the thermal effect and thermal distribution [8–11]. Evaporation of water prior to sintering is also an important part in laser assisted manufacturing. Hasan and Monde reviewed the homogeneous nucleation boiling phenomena under different non-equilibrium heating condition and summarize their boiling explosion time, which can vary from 0.173 μs to 0.723 ms [12]. This type of information is important to assess for an irradiated droplet in transit since explosion could occur before the droplet reaches the substrate [13,14]. Continuous laser heating on sessile or levitated drop is also used to affect the solute precipitation patterns after solvent evaporation by tuning laser intensity, irradiation time and absorption of the droplet [15–18]. Pendleton as well as Park et al. modeled the temperature distribution in a water droplet irradiated by pulsed carbon dioxide laser analytically [19,20], plotted the isothermal temperature contour at the theoretical superheated limit for nucleation boiling and defined the fast and slow heating regime to illustrate the explosive vaporization patterns in Kafalas and Ferdi-

Nomenclature

λ	Laser wavelength
f	Laser repetition rate
t_{on}	Laser pulse width
t_p	Laser period
n_p	Number of laser pulses
I	Laser intensity distribution in diffraction-free range
I_0	Peak intensity of laser pulse
J_n	Bessel function of the first kind with order of n
k_r	Radial wave vector
k_z	Wave vector in laser propagation direction
r	Radial distance of spherical coordinates
θ	Polar angle of spherical coordinates
Φ	Time distribution of the laser pulse pattern
t	Time elapse
T	Temperature of droplet
T_{amb}	Ambient temperature
g	Energy generation in droplet
k	Thermal conductivity of droplet
α	Thermal diffusivity
μ	$\cos\theta$
h	Heat convection coefficient
T_0	Saturated temperature of water
T^*	$(T - T_{amb})/(T_0 - T_{amb})$, dimensionless temperature
t^*	$\alpha t/r_0$, dimensionless time
Bi	hr_0/k, Biot number
r_0	Radius of the droplet
r^*	r/r_0, dimensionless radial coordinate
θ_1	Incidence angle
θ_2	Refracted angle
n_{drop}	Refractive index of droplets
n_{air}	Refractive index of air
n_r	n_{drop}/n_{air}, refractive index ratio
I_P	Laser intensity at point P
g^*	$\frac{gr_0^2}{k(T_0 - T_{amb})}$, dimensionless energy generation
V^*	$r^{*\frac{1}{2}}T^*$
$\overline{V^*}$	Integral transform of V^* in μ
$\widetilde{V^*}$	Integral transform of $\overline{V^*}$ in r
$\overline{g^*}$	Integral transform of g^* in μ
$\widetilde{g^*}$	Integral transform of $\overline{g^*}$ in r
P_n	Legendre polynomial of degree n
j_n	Spherical Bessel function of the first kind of order n
λ_{nm}	Eigen values
$N(n)$	Norm of P_n
$N(\lambda_{nm})$	Norm of $J_{n+\frac{1}{2}}$
g_s	Energy generation without refraction

nands experiments [21]. Shusser and Weihs modeled a single bubble growth initiating from the center of a water drop and matched their prediction with experimental observation [22]. Upon measuring the superheating rate and bubble growth during pulsed-laser induced boiling process by optical probing, it was shown that the bubble growth threshold superheating degree should be approximately 100–123 K higher than the saturation temperature [23]. The studies on pulsed infrared laser heating of water jet by shadowgraphy and Raman spectroscopy show a possible explosive boiling time of 500 ns to 10 μs [23,24]. For the pulsed laser-heating droplet behavior, a series of studies is done by Armstrong et al. to measure the explosion and breakdown thresholds for droplets of different sizes and different materials as well as the delayed time prior to droplet explosion [25–27]. A series of studies has also been done by Josyula et al. and Askounis et al. [28,29] to examine the effect of localized laser heating of droplet on the Marangoni flow and the resultant evaporation kinetics. However, the pulsed infrared laser heating effect on nanosuspension droplet in mid-air during deposition on a substrate has not been studied.

An additive method called the nanoelectrospray laser deposition process was reported in which an aqueous ink was used as a precursor to produce microdroplets ejected from an electrospray [1]. A laser beam is then directed on the droplets to evaporate the liquid and sinter the nanoparticles. It is essential that these droplets do not explode in mid-air due to overheating or bounce off on the substrate due to Leidenfrost phenomenon. This paper develops an analytical model supported by experiments to predict the slow evaporation and/or explosive behaviors of droplet suspensions with different optical properties at a given laser intensity.

2. Experiment setup

The nanoparticle suspension is delivered through the capillary tube from the syringe pump at a constant flow rate of 20 μL/min (Fig. 1). The capillary tube penetrates through a hole in the parabolic mirror. The distance between the tip of the capillary tube to the substrate is kept at 8mm, and a high voltage ranging from 2.8 kV to 3.3 kV is supplied for different suspensions. A high electric field between the capillary tube and the silicon substrate is formed and creates a conical meniscus at the tip of the capillary tube, forming $\sim$100 μm diameter microdroplets. A pulsed infrared laser (wavelength, $\lambda = 1064$ nm, pulse width, $t_{on} = 170$ ns, laser repitition rate, $f = 30$ kHz) passes through an axicon lens and a biconvex lens which creates a hollow beam. This beam is reflected by a parabolic mirror, focusing the conical beam on a silicon substrate. At the substrate, the original Gaussian laser beam is converted to a Bessel beam pattern with a 0.52 mm spot diameter and a diffraction-free range of 0.5 mm [30]. A Phantom v12.1 high-speed camera is focused near the silicon substrate to capture the microdroplet behavior within the diffraction-free range of the laser. The speed of the camera varies from 6300 frames per second (159 μs interval) with 1280 × 800 resolution to 341000 frames per second (2.93 μs interval) with 64 × 64 resolution for capturing high resolution and time resolved sequence.

The specific objective is to test the behavior of four different droplet suspensions [20 wt% silver nanoparticle suspension (Ag20), 10 wt% germanium nanoparticle suspension (Ge10), 5 wt% germanium nanoparticle suspension (Ge5) and 8mM SDS solution (SDS)] of 100 μm diameter ejected from the piezoelectric capillary needle towards the Si substrate illuminated by pulsed infrared laser. The physical properties, thermal properties and optical properties such as reflectance and absorption coefficient of these suspensions are provided in Table 1.

3. Analytical model

This previously unreported experiment in droplet explosion is due to the optical properties of the suspension. To verify the results from the experiments, an analytical transient heat conduction model is developed to calculate the temperature distribution in the microdroplet under a pulsed Bessel beam. As shown in Fig. 2, this pulsed Bessel beam illuminates the falling microdroplet vertically and concentrically and induces possible droplet explosion in the diffraction-free range.

The spatial and time distribution of the laser intensity is written as:

$$I(r, \theta, t) = I_0 J_0^2(k_r r \sin\theta)\Phi(t) \tag{1}$$

where r and θ are the spherical coordinates used in this problem. I_0 is the peak intensity of the laser placed on top of the droplet center. J_0 is the Bessel function of the first kind of zero order.
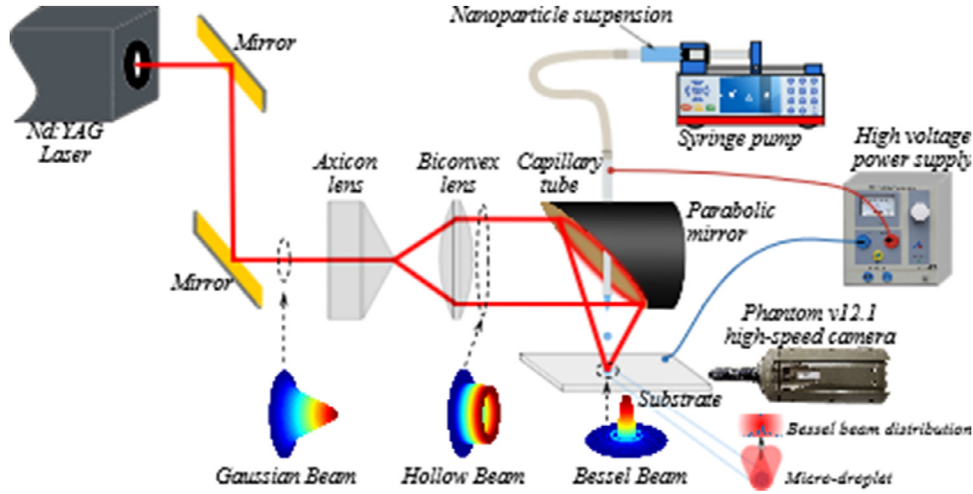
Fig. 1. Schematic of the experiment. Nanoparticle suspension is supplied through the capillary tube and drip down as microdroplets. The Nd:YAG laser beam goes through an axicon lens, a biconvex lens and is focused by a parabolic mirror on the substrate. A Phantom v12.1 high-speed camera focused near the substrate captures the droplet behavior within the diffraction-free range of the Bessel beam.

Table 1
Fluid properties, optical properties and thermophysical properties of different nanoparticle suspensions at wavelength $\lambda = 1064$ nm. The thermal properties of SDS, Ge5, Ge10 and Ag20 is calculated in the temperature range of 20 °C, 20–40 °C, 20–60 °C and 20–300 °C.

| Sample ID	Density, ρ (g/ml)	Viscosity, M (cP)	Surface tension, σ (mN/m)	Reflectance, R (%)	Absorption coefficient, γ (cm^{-1})	Refractive index, n_{drop}	Thermal conductivity [31], k(Wm^{-1}K^{-1})	Thermal diffusivity [31], α (mm^2/s)
Ag20	1.153	1.71 ± 0.03	47.2 ± 0.1	6	100	1.377	10.05-10.49	2.43-2.54
Ge10	1.130	1.95 ± 0.02	47.6 ± 0.1	35	7.70	1.358	1.70-1.77	0.42-0.43
Ge5	1.064	1.56 ± 0.01	47.5 ± 0.1	42	4.17	1.340	1.16-1.18	0.28-0.29
SDS	1.000	1.10 ± 0.01	49.8 ± 0.1	48	0.20	1.330	0.60	0.14
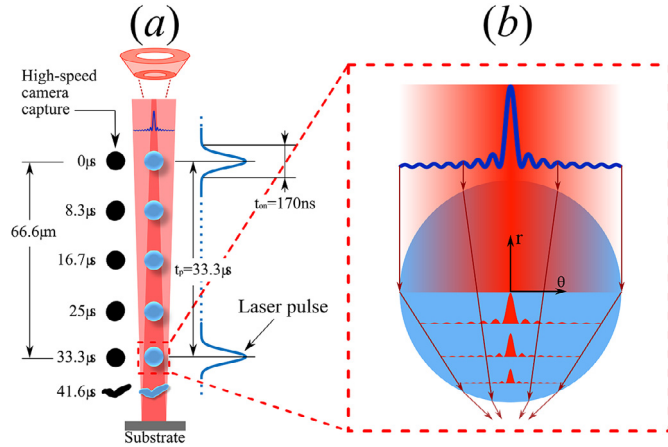
Fig. 2. Schematic of pulsed Nd:YAG laser beam illuminated on the droplet of nanoparticle suspension falling down to the substrate within the diffraction-free range. The hollow beam focused by the parabolic mirror forming a Bessel beam near the substrate. (a) When the droplet falls down with an average speed of 2 m/s, it is illuminated by this Bessel beam of a pulse on-time, $t_{on} = 170$ ns for each pulse period, $t_p = 33.3$ μs periodically. (b) The laser beam is refracted and absorbed by the droplet simultaneously when it passing through the droplet, which can be described and modeled by using a 2D spherical coordinates in radial distance r and polar angle θ.

k_r is the radial wave vector given by $k_r = \sqrt{(2\pi/\lambda)^2 - k_z^2}$, where k_z is the wave vector in the laser propagation direction and λ is the wavelength of the laser. k_r is taken as $2\pi/\lambda$ in this study at the diffraction-free region of the Bessel beam. The envelope of the Bessel beam intensity maxima decreases radially in inverse proportion to $k_r r$. The central high intensity spot reduces to its minimum possible diameter 0.77λ when $k_r = 2\pi/\lambda$. $\Phi(t)$ is the time distri-

bution of the laser representing the pulse pattern:

$$\Phi(t) = \begin{cases} \frac{t-(n_p-1)t_p}{0.5t_{on}}, & (n_p-1)t_p \leq t \leq (n_p-1)t_p+0.5t_{on} \\ \frac{t_{on}+(n_p-1)t_p-t}{0.5t_{on}}, & (n_p-1)t_p+0.5t_{on} \leq t \leq (n_p-1)t_p+t_{on} \\ 0, & (n_p-1)t_p+t_{on} \leq t \leq n_p t_p \end{cases} \tag{2}$$

with $n_p = 1, 2, 3, \cdots$ is the total number of pulses irradiating on the droplet, t_{on} and t_p are the time for which the pulse is on and the laser period (pulse on + pulse off) respectively.

As the droplet falls, the effect of flow inside is neglected. The droplet shape is also assumed to be spherical. With no convection, the current model conservatively predicts the least power at which explosion occurs. At any power below the predicted power of the model, explosion is not expected to occur.

The droplet is semi-transparent and the laser thermal effect to the droplet is modeled as a volumetric heating source inside the droplet. The governing equation, boundary conditions and initial condition of the analytical model can be expressed as:

$$\frac{\partial^2 T}{\partial r^2} + \frac{2}{r}\frac{\partial T}{\partial r} + \frac{1}{r^2 \sin\theta}\frac{\partial}{\partial \theta}\left(\sin\theta \frac{\partial T}{\partial \theta}\right) + \frac{g\Phi}{k} = \frac{1}{\alpha}\frac{\partial T}{\partial t} \tag{3}$$

$$T(r = 0) = \text{finite} \tag{4}$$

$$-k\frac{\partial T}{\partial r}\bigg|_{r=r_0} = h(T - T_{amb})\bigg|_{r=r_0} \tag{5}$$

$$T(\theta = 0) = \text{finite} \tag{6}$$

$$T(\theta = \pi) = \text{finite} \tag{7}$$

$$T(t = 0) = T_{amb} \tag{8}$$

where r and θ represent the radial distance and polar angle of the spherical coordinates, respectively. T_{amb} is the ambient temperature set to be $20°C$ and g is the energy generation inside the droplet due to laser. More details are given in Appendix A.

By applying integral transformation [32], The dimensionless temperature in the droplet, $T^* = (T - T_{amb})/(T_0 - T_{amb})$, where $T_0 = 100°C$ is the saturated temperature, can be solved as:

$$T^*(r^*, \mu, t^*) = \sum_{n=0}^{\infty} \sum_{m=1}^{\infty} (2n+1) P_n(\mu) \sqrt{\frac{2\lambda_{nm}}{\pi}}$$
$$\times \frac{j_n(\lambda_{nm} r^*)}{J_{n+\frac{1}{2}}^2(\lambda_{nm})} \frac{\lambda_{nm}^2 \cdot \widetilde{V}^*(\lambda_{nm}, n, t^*)}{Bi - \frac{1}{2} + \lambda_{nm}^2 - (n - \frac{1}{2})^2} \qquad (9)$$

where $P_n(\mu)$ is the Legendre polynomial of degree n, $J_{n+\frac{1}{2}}(\lambda_{nm})$ is the Bessel function of the first kind of order $n + \frac{1}{2}$, $j_n(\lambda_{nm} r^*)$ is the spherical Bessel function of the first kind of order n, and λ_{nm} is determined from:

$$(Bi + n) J_{n+\frac{1}{2}}(\lambda_{nm}) - \lambda_{nm} J_{n+\frac{3}{2}}(\lambda_{nm}) = 0 \qquad (10)$$

$$\widetilde{V}^*(\lambda_{nm}, n, t^*) = \frac{\widetilde{g}^*(\lambda_{nm}, n)}{\lambda_{nm}^2}$$
$$\times \int_{\tau^*=0}^{t^*} \left[1 - e^{-\lambda_{nm}^2(t^*-\tau)}\right] \frac{d\Phi(\frac{r_0^2}{\alpha}\tau^*)}{d\tau^*} d\tau^* \qquad (11)$$

with

$$\widetilde{g}^*(\lambda_{nm}, n) = \int_{r^*=0}^{1} \int_{\mu'=-1}^{1} r^{*\frac{3}{2}} J_{n+\frac{1}{2}}\left(\lambda_{nm} r^{*\prime}\right)$$
$$\times P_n(\mu') g^*\left(r^{*\prime}, \mu'\right) d\mu' dr^{*\prime} \qquad (12)$$

$$g^* = \frac{g \cdot r_0^2}{k(T_0 - T_{amb})} \qquad (13)$$

The detailed steps for solving Eq. (3) and a comparison between solutions with or without refraction are addressed in Appendix B and Appendix C, respectively.

4. Results and discussion

At a laser repetition rate of 30 kHz, the laser power is increased gradually from $P = 0$ W to $P = 50$ W. At different laser power, slow evaporation and mid-air explosion occur in the Ag20 droplet sequentially.

The thermophysical properties, such as thermal conductivity and thermal diffusivity of the droplets used in the calculation are the average values, which are listed in Table 1. The temperature distribution in majority of the droplets falls in the ranges of $20°C$, $20–40\ °C$, $20–60\ °C$ and $20–300\ °C$ for SDS, Ge5, Ge10 and Ag20 droplets, respectively. The thermophysical properties are appropriately calculated.

4.1. Slow evaporation

When the laser power P reaches 9 W, illuminated in the diffraction-free range, the Ag20 droplet is observed to vaporize in mid-air.

As shown in Fig. 3, the sequence of Ag20 droplet slow evaporation in the laser diffraction-free range is captured by the high-speed camera at 181,800 frames per second (5.5 μs interval) and 2 μs explosure time. After 16.65 μs, the Ag20 droplet starts to vaporize with a diameter reduction from 92 μm to 55 μm. For the other droplet suspensions, the dramatic decrease in diameter is not observed at any time.
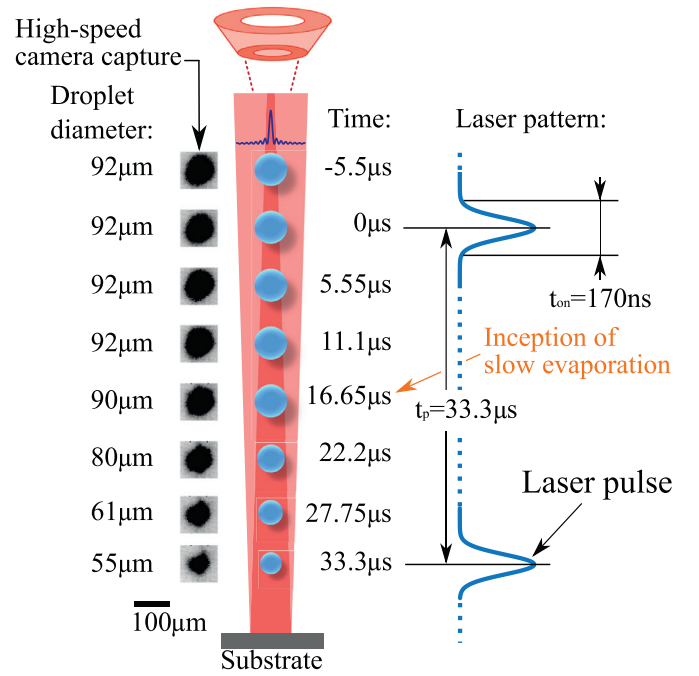

Fig. 3. The time sequence of the Ag20 droplet before it hits the substrate. Slow evaporation is shown for a laser power of 9 W and repetition rate of 30 kHz.

From 0 μs to 16.65 μs, no significant change in droplet diameter is observed, which indicates that the evaporation is weak and its effect on temperature distribution is neglected.

The temperature distribution in Ag20 droplet for $I_0 = 4$ GW/cm^2, corresponding to laser power of 9 W at 30 kHz repetition rate, is evaluated by the analytical model. By substituting I_0, reflectance, absorption coefficient as well as the refractive index for Ag20 from 170 ns to the evaporation inception time of $t = 16.65$ μs into Eq. (9), the maximum temperature and temperature distribution in Ag20 droplet for slow evaporation is calculated and shown in Fig. 4.

The highest temperature in the Ag20 droplet, which appears at the top center, drops from 859 °C to 78 °C, forming no vapor or bubble inside the droplet since the boiling point is not reached at the evaporation inception time. The change in drop size at different times is not captured by this model.

4.2. Mid-air explosion

When the laser power is less than 6.5 W, there is no droplet explosion for any of the four nanosuspensions, and each of the droplets enters the diffraction-free range between 0 μs and 159 μs, and settles down on the substrate at 319 μs (Fig. 5a). However, as the laser power is increased to 30 W (Fig. 5b), Ag20 droplet explodes in midair at the laser intersection in the diffraction-free range, while the other three types of droplets settle down on the substrate without exploding. Note from Table 1 that Ag20 has lower reflectance and higher absorption coefficient, which tend to increase the energy absorption in the droplet leading to explosion. Similar to the Ge5 and Ge10 suspensions, the droplets of 20wt% germanium nanoparticle suspension will not explode because this suspension has higher reflectance (28%) and lower absorption coefficient (15.75cm^{-1}) than Ag20 suspension. The effects of reflectance and absorption coefficients will be quantified later using a conduction model.

The explosion sequences for Ag20 droplet show the three images of an unaffected droplet at -1.1 μs(Fig. 5c), an image at 1.83 μs with a slight protrusion and lastly an image at 4.76 μs
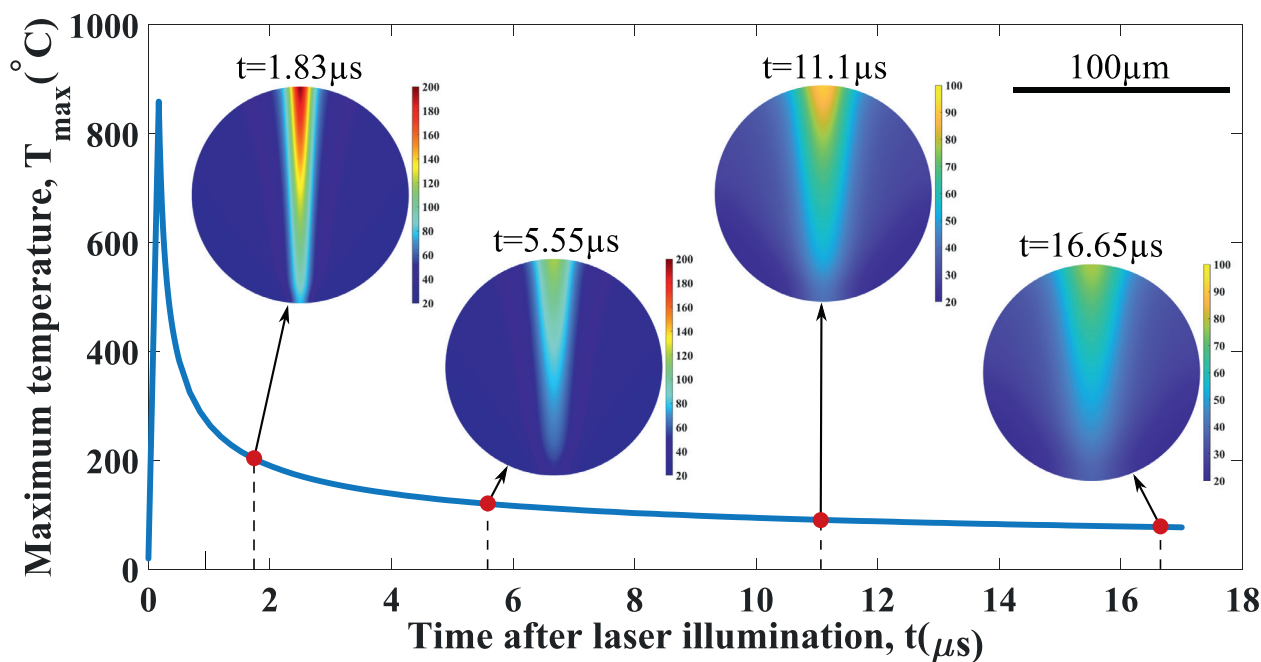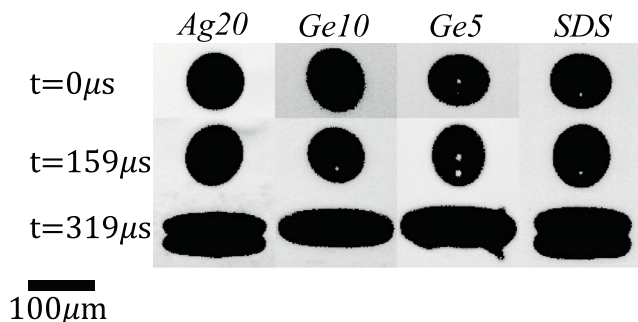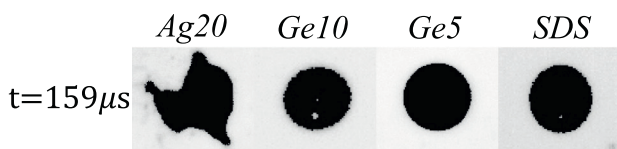
Fig. 4. Maximum temperature in Ag20 droplet with $I_0 = 4\,GW/cm^2$ corresponding to Ag20 droplet slow evaporation ($P = 9\,W$, repetition rate = 30 kHz) at different times prior to significant drop size reduction with temperature distribution in Ag20 droplet at 1.83 μs, 5.55 μs, 11.1 μs and 16.65 μs, respectively. Ag20 droplet diameter = 100 μm.
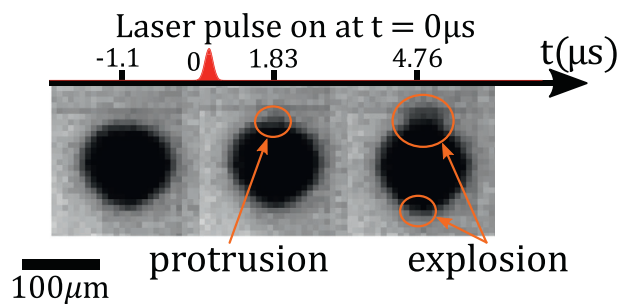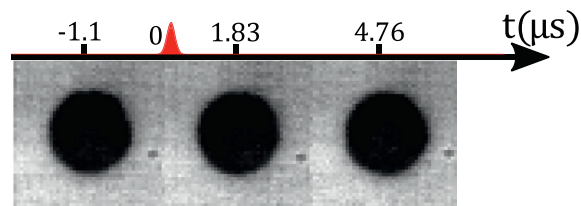

Fig. 5. Droplet behavior of different nanoparticle suspensions under low and high laser powers. The left scale bar is for (*a*) and (*b*) and the right scale bar is for (*c*) and (*d*). (*a*) Time sequence for all types of nanoparticle suspension under laser power to be 6.5 W. No explosion for all kind of droplets. (*b*) Droplet behaviors for all types of nanoparticle suspension illuminated by laser with 30 W power. Only Ag20 droplet encounters explosion in mid-air. (*c*) Ag20 droplet explosion sequence under 30 W laser power for a time interval of 2.93 μs. The time axis on top of the droplet with the laser pulse indicator shows the time, t = 0, at which the laser beam begins to illuminate the droplet. (*d*) Time resolved shape of SDS droplet under 30 W laser power for a time interval of 2.93 μs. The time axis on top of the droplet with the laser pulse indicator shows the time at which the laser beam illuminates the droplet. Time resolved shapes of Ge5 and Ge10 droplets are similar to that of SDS.

at the onset of explosion (Fig. 5c). This indicates that the delayed time prior to explosion when bubble growth inside the droplet occurs is ~1.83 μs. The delayed explosion time is due to the dynamics of bubble growth in the microdroplet [23]. Nucleation occurs when the boiling condition is reached in the droplet, and bubbles grow in size only if sufficient heat is supplied. It is assumed that the droplet explodes when a critical number of bubbles of critical size form in a finite time t [27]. This delayed explosion time scale is measured in a laser-heated droplet experiment and the delayed explosion time in our study agrees with their time scale [27]. The high-speed capture of explosion for Ag20 droplet in our experiment clearly shows that a single laser pulse is sufficient for droplet explosion.

The high-speed capture of time resolved SDS droplet shape is shown in Fig. 5d and it clearly shows that no explosion occurs for this droplet even at 30 W laser power. The Ge5
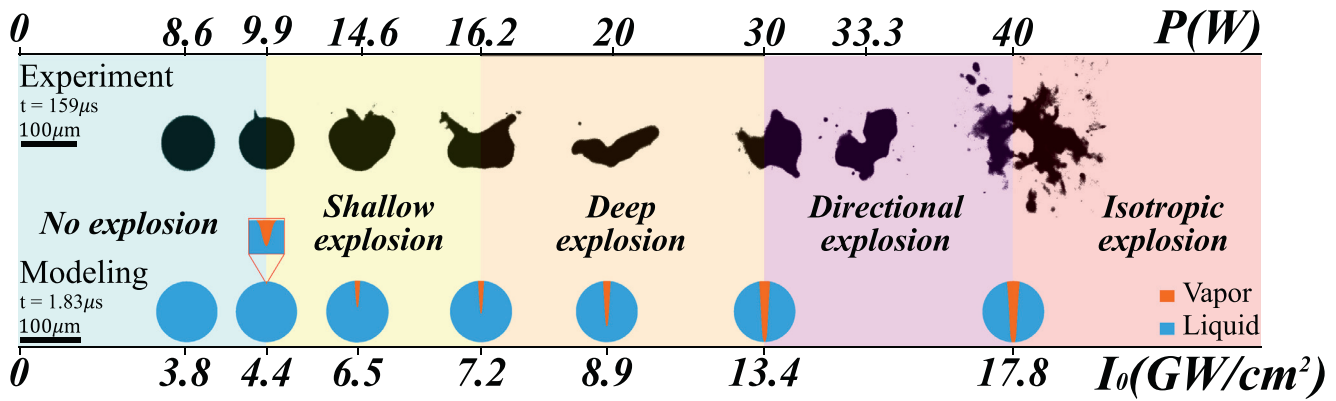
Fig. 6. Ag20 droplet explosion regime map. The experiments were done at a repetition rate of 30 kHz. The experimental images of droplet explosion are shown on top in black. The analytical model predictions of vapor generation are shown at the bottom in blue and orange. Laser power, P increases in experiments gradually to conduct different explosion patterns for Ag20 droplet, while I_0 corresponding to P is calculated and used in analytical model to find out the explosion region in Ag20 droplet.
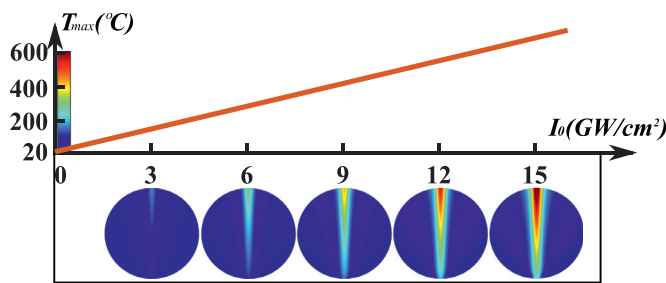

Fig. 7. Maximum temperature and temperature distribution in Ag20 droplet with I_0 increasing to 15 GW/cm² at time 1.83 μs after one pulse. The maximum temperature of the entire droplet appears at the center of top surface. Obviously, higher I_0 leads to higher maximum temperature. The super heated region is shown in range in the simulations. Ag20 droplet diameter = 100 μm.

Fig. 8. Maximum temperature and temperature distribution in Ge10, Ge5 and SDS droplets with I_0 increasing to 15 GW/cm² at time 268.47 μs corresponding to 1.83 μs after eight pulses. The maximum temperature of the entire droplet appears at the center of top surface. Maximum temperature and temperature distribution increase with I_0, but the super heated region is not observed and therefore the explosion is not predicted for these 3 droplets. All droplet diameters are 100 μm.

and Ge10 droplet time resolved shapes are also similar to that of SDS.

I_0 is increased from 0 to 22.3 GW/cm² corresponding to P increasing from 0 to 50 W with a repetition rate of 30 kHz. Four different types of explosion patterns for Ag20 droplet are observed (labeled in different color in Fig. 6): shallow, deep, directional and isotropic explosion separated by four laser intensity thresholds. The threshold values for shallow explosion, deep explosion, directional explosion and isotropic explosion are 4.4 GW/cm², 7.2 GW/cm², 13.4 GW/cm² and 17.8 GW/cm² respectively. In shallow explosion regime, the droplet explosion region is shallow and moves from the top to the center. For deep explosion regime, the explosion pattern is deep, with the expansion moving further from the center to the bottom. For directional explosion regime, the explosion is directional from top to bottom penetrating along the droplet axis. For isotropic explosion regime, the droplet explodes violently and isotropically from the droplet interior, and breaks up into fragments in all directions.

By substituting I_0, reflectance, absorption coefficient as well as the refractive index for Ag20 to Eq. (3) with the initial bubble formation time $t = 1.83$ μs into Eq. (9), the temperature distribution in Ag20 droplet under different I_0 is calculated (Fig. 7).

Superheating is shown to occur in experiments due to laser pulsed heating as well as in analytical modeling which leads to the explosion of the droplet with $I_0 \geq 4.4$ GW/cm². Superheating of 110°C ($T_{th} = 210$°C) under atmosphere, corresponding to Park et al.s experimental observation is set to be the vapor formation threshold in the droplet [23]. The region with $T > T_{th}$ is considered to be the vapor region where the minimum saturated pressure reaches 1.9 MPa, which corresponds to droplet explosion (Fig. 6).
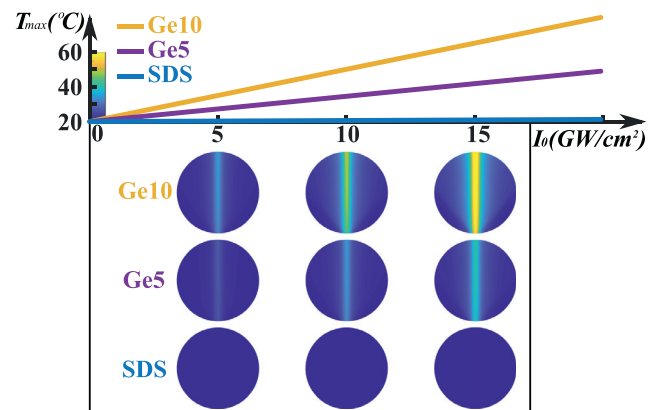
The experimental and predicted explosion patterns of the Ag20 droplet are shown together in Fig. 6. By considering 110°C superheat as the explosion threshold, the analytically predicted Ag20 explosion pattern matches the experimental results very well.

The theoretical modeling results displaying vapor formation in Ag20 droplet (Fig. 6) capture the depth of vapor penetration within the droplet at different laser peak intensity and predict the experiments very well. The Ag20 droplet explosion patterns are aligned well with the vapor regions although the asymmetry cannot be predicted by the model. When no vapor region is predicted by the model, no explosion occurs in the experiment as well. Vapor develops as a small region at the top and penetrates to the bottom of the droplets. This represents the transition from shallow explosion to deep explosion, then to directional and isotropic explosion in sequence as the laser intensity is increased.

The experimental results for three other droplets display no explosion after a single pulse or eight pulses in the laser diffraction-free range for different laser peak intensities. Due to their high reflectance and low absorption coefficients (Table 1), these droplets simply settle down on the substrate as a thin film without exploding. In the theoretical model, this can be investigated by plotting the maximum temperature as well as their temperature distribution after eight pulses at different laser peak intensities, I_0 (Fig. 8).

Shown in Fig. 9, the maximum temperature for each type of droplet increases linearly with I_0, however, the maximum temper-
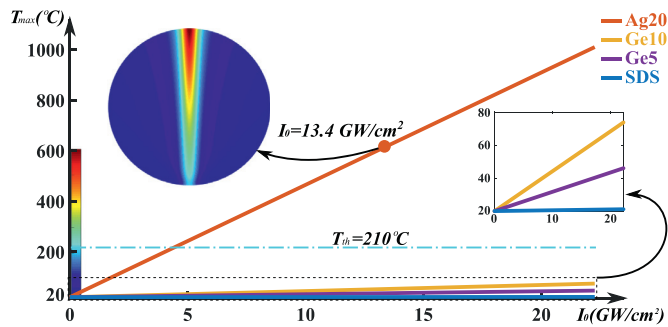
Fig. 9. Maximum temperature plots for all four types of droplet. Only the maximum temperature in Ag20 droplet goes beyond the threshold temperature for explosion $T_{th} = 210\,°C$. Other droplets shows maximum temperature less than $80\,°C$ and thus no explosion is predicted. Ag20 droplet diameter = 100 μm.

atures in Ge10, Ge5 and SDS droplets do not reach the threshold temperature for explosion, $210\,°C$ [23], even for $I_0 = 22.3\,GW/cm^2$ which corresponds to laser power of $50\,W$, and hence these droplets do not explode. While under the same I_0, Ag20 droplet, which has low reflectance and high absorption coefficient, reaches $\sim 1000\,°C$ and shows a high propensity to explode. Among these four types of droplet, only Ag20 displays the vapor region at $I_0 = 13.4\,GW/cm^2$ ($30\,W$), matching the experimental results shown in Fig. 5.

In summary, it is demonstrated experimentally and analytically that optical properties play a major role in droplet explosion when the droplets are illuminated by a pulsed infrared laser of Bessel distribution. Four types of droplet suspension of different reflectance and absorption coefficients were investigated. Only the $20\,wt\%$ silver nanoparticle suspension droplet with low reflectance and high absorption explodes, which is corroborated by our model. High-speed camera images display multiple stages of explosion beyond $1.83\,μs$. The theoretical conduction model shows its competence and adequacy by matching the vapor regions at temperatures greater than the threshold temperature in the droplet at different times and laser peak intensities. This model is important in determining *a priori* the maximum laser peak intensity below which droplet explosion will not occur and the particles in the droplet can be sintered on the substrate. In the case of $20\,wt\%$ silver nanoparticle suspension, the threshold laser peak intensity is $4.4\,GW/cm^2$ which is corroborated by the experiment.

The authors declare the following financial interests/personal relationships which may be considered as potential competing interests:

Declaration of Competing Interest

The authors declare that they have no known competing financial interests or personal relationships that could have appeared to influence the work reported in this paper.

CRediT authorship contribution statement

Tianyi Li: Methodology, Software, Validation, Formal analysis, Investigation, Writing - original draft. **Aravinda Kar:** Resources, Conceptualization, Writing - review & editing. **Ranganathan Kumar:** Resources, Project administration, Supervision, Writing - review & editing.
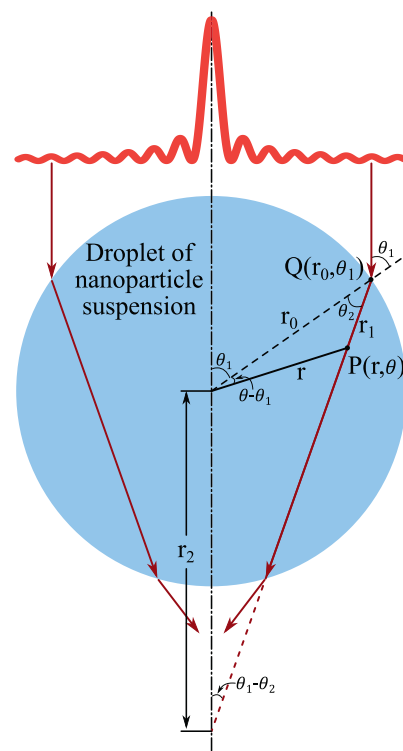
Acknowledgements

Fig. 10. Schematic of laser propagating inside the microdroplet.

Appendix A. Model of energy generation inside the microdroplet, g(r, θ)

The schematic of laser propagation across the microdroplet is shown in Fig. 10. The laser beam propagates downward vertically and gets refracted at the droplet top surface. With the beam propagating inside the microdroplet, its laser energy is absorbed by the droplet along the whole laser path which results in internal heating.

To find out the internal heating or energy generation inside the microdroplet, g, consider an arbitrary laser beam shining at a point $Q(r_0, \theta_1)$ on the microdroplet top surface, where θ_1 corresponds to the incidence angle. This laser beam is refracted by the droplet with refractive angle, θ_2 and passes through a point $P(r, \theta)$ inside the droplet. By applying Snell's law [33], the relationship between θ_1 and θ_2 can be expressed as:

$$n_{air} \sin\theta_1 = n_{drop} \sin\theta_2 \implies \sin\theta_2 = \frac{\sin\theta_1}{n_r} \qquad (14)$$

where n_{air} represents the refractive index of the air which is 1.0003 and n_{drop} represents the refractive index of the microdroplet which is listed in Table 1. $n_r = n_{drop}/n_{air}$ is the ratio of the refractive index.

Knowing the coordinates of the point P, (r, θ), the droplet radius, r_0, and the refractive index ratio n_r, the law of sines can be written as

$$\frac{r}{\sin\theta_2} = \frac{r_0}{\sin(\theta_2 + \theta - \theta_1)} \qquad (15)$$

Substituting Eq. (14) into Eq. (15),

$$\frac{r_0}{r} = \cos(\theta - \theta_1) + \sin(\theta - \theta_1)\sqrt{\frac{n_r^2}{\sin^2\theta_1} - 1} \qquad (16)$$

Applying the law of sines again to get the distance, r_1, between the point $P(r, \theta)$ and $Q(r_0, \theta_1)$,

$$r_1 = \frac{r}{\sin\theta_2}\sin(\theta - \theta_1) = \frac{n_r \sin(\theta - \theta_1)}{\sin\theta_1}r \qquad (17)$$

Extending the line QP to intersect the axis of symmetry of the droplet and defining the distance from this intersection to the droplet center as r_2, the ratio of r_2 and r_0 can be found by applying the law of sines as follows:

$$\frac{r_2}{r_0} = \frac{\sqrt{(n_r^2 - 1) + \cos^2 \theta_1} + \cos \theta_1}{n_r^2 - 1} \tag{18}$$

The value of r_2/r_0 can be seen to decrease with θ_1 increasing when $\theta_1 \in [0, \frac{\pi}{2}]$. Thus,

$$\frac{r_2}{r_0} \geq \left.\frac{r_2}{r_0}\right|_{\theta_1 = \frac{\pi}{2}} = \frac{1}{\sqrt{n_r^2 - 1}} \tag{19}$$

$r_2 > r_0$ represents no laser beam intersection in the droplet which requires:

$$\frac{1}{\sqrt{n_r^2 - 1}} > 1 \implies n_r < \sqrt{2} \tag{20}$$

In the current case, the maximum microdroplet refractive index is for Ag20, giving $n_r = 1.377 < \sqrt{2}$, thus the energy generation in the droplet can be calculated by geometric optics. By considering the reflectance and refraction of the droplet and applying Beer-Lambert law [34], the laser intensity at point $P(r, \theta)$ can be expressed as:

$$I_P(r, \theta, t) = \frac{(r_0 \sin \theta_1)^2}{(r \sin \theta)^2} (1 - R) I_0 e^{-\gamma r_1} J_0^2(k_r r_0 \sin \theta_1) \Phi(t) \tag{21}$$

While the energy generation $g(r, \theta)$ is obtained by taking the derivative of I_P in the minus r_1 direction:

$$\begin{aligned} g(r, \theta, t) &= -\frac{\partial I_P}{\partial r_1} \\ &= \frac{(r_0 \sin \theta_1)^2}{(r \sin \theta)^2} (1 - R) I_0 \gamma e^{-\gamma r_1} J_0^2(k_r r_0 \sin \theta_1) \Phi(t) \end{aligned} \tag{22}$$

where R and γ represent the reflectance and absorption coefficients of the microdroplet which are listed in Table 1. $\theta_1 = \theta_1(r, \theta)$ which can be found from Eq. (16) by implicitly knowing r and θ. r_1 is calculated by Eq. (17) knowing r, n_r and θ_1. I_0 is the laser peak intensity and can be calculated by:

$$\begin{aligned} I_0 &= \frac{2P}{f \cdot t_{on} \int_0^{R_0} \int_0^{2\pi} J_0^2(k_r \rho) \rho \, d\phi \, d\rho} \\ &= \frac{2P}{\pi R_0^2 \left[J_0^2(k_r R_0) + J_1^2(k_r R_0) \right] f \cdot t_{on}} \end{aligned} \tag{23}$$

where P, f and t_{on} are the power, repetition rate and pulse on-time of the laser. R_0 is the laser spot radius. ρ and ϕ are the radial and azimuthal coordinates in polar coordinates used to describe the Bessel laser beam profile, where $\rho = r \sin \theta$.

Appendix B. Solution of the analytical model

The governing equation, boundary conditions and initial condition are non-dimensionalized by $\mu = \cos \theta$, $r^* = r/r_0$, $t^* = \alpha t/r_0^2$ and $T^* = (T - T_{amb})/(T_0 - T_{amb})$, where $r_0 = 50$ µm is the radius of the microdroplet, α is the thermal diffusivity, $T_0 = 100\,°C$ is the saturated temperature and $T_{amb} = 20\,°C$ is the ambient temperature. The dimensionless equations are:

$$\frac{\partial^2 T^*}{\partial r^{*2}} + \frac{2}{r^*} \frac{\partial T^*}{\partial r^*} + \frac{1}{r^{*2}} \frac{\partial}{\partial \mu} \left[(1 - \mu^2) \frac{\partial T^*}{\partial \mu} \right] + g^* \Phi^* = \frac{\partial T^*}{\partial t^*} \tag{24}$$

$$T^*(r^* = 0) = \text{finite} \tag{25}$$

$$\left. \left(Bi \cdot T^* + \frac{\partial T^*}{\partial r^*} \right) \right|_{r^*=1} = 0 \tag{26}$$

$$T^*(\mu = 1) = \text{finite} \tag{27}$$

$$T^*(\mu = -1) = \text{finite} \tag{28}$$

$$T^*(t^* = 0) = 0 \tag{29}$$

where

$$g^* = \frac{g \cdot r_0^2}{k(T_0 - T_{amb})} \tag{30}$$

$$\Phi^*(t^*) = \Phi(t) = \Phi(\frac{r_0^2}{\alpha} t^*) \tag{31}$$

$$Bi = \frac{hr_0}{k} \tag{32}$$

A new variable $V^* = r^{*\frac{1}{2}} T^*$ is defined for solution of Eq. (24). The modified governing equation, boundary conditions and initial condition are:

$$\begin{aligned} &\frac{\partial^2 V^*}{\partial r^{*2}} + \frac{1}{r^*} \frac{\partial V^*}{\partial r^*} - \frac{1}{4} \frac{V^*}{r^{*2}} + \frac{1}{r^{*2}} \frac{\partial}{\partial \mu} \left[(1 - \mu^2) \frac{\partial V^*}{\partial \mu} \right] \\ &\quad + r^{*\frac{1}{2}} g^* \Phi^* = \frac{\partial V^*}{\partial t^*} \end{aligned} \tag{33}$$

$$V^*(r^* = 0) = 0 \tag{34}$$

$$\left. \left[\left(Bi - \frac{1}{2r^*} \right) V^* + \frac{\partial V^*}{\partial r^*} \right] \right|_{r^*=1} = 0 \tag{35}$$

$$V^*(\mu = 1) = \text{finite} \tag{36}$$

$$V^*(\mu = -1) = \text{finite} \tag{37}$$

$$V^*(t^* = 0) = 0 \tag{38}$$

The integration pair in θ direction is:

$$V^*(r^*, \mu, t) = \sum_{n=0}^{\infty} \frac{1}{N(n)} P_n(\mu) \overline{V^*}(r^*, n, t) \tag{39}$$

$$\overline{V^*}(r^*, n, t) = \int_{\mu'=-1}^{1} P_n(\mu') V^*(r^*, \mu', t) \, d\mu' \tag{40}$$

where $N(n)$ is the norm of Legendre polynomial of the first kind of degree n,

$$N(n) = \int_{\mu'=-1}^{1} P_n^2(\mu') \, d\mu' = \frac{2}{2n + 1} \tag{41}$$

Apply the integration $\times \int_{\mu'=-1}^{1} P_n(\mu') \, d\mu'$ to the governing Eq. (33), boundary conditions Eqs. (34)–(35) and initial condition Eq. (29) to yield:

$$\frac{\partial^2 \overline{V^*}}{\partial r^{*2}} + \frac{1}{r^*} \frac{\partial \overline{V^*}}{\partial r^*} - \frac{(n + \frac{1}{2})^2}{r^{*2}} \overline{V^*} + \overline{g^*} \Phi^* = \frac{\partial \overline{V^*}}{\partial t^*} \tag{42}$$

$$\overline{V^*}(r^* = 0) = 0 \tag{43}$$

$$\left. \left[\left(Bi - \frac{1}{2r^*} \right) \overline{V^*} + \frac{\partial \overline{V^*}}{\partial r^*} \right] \right|_{r^*=1} = 0 \tag{44}$$

$$\overline{V}^*(t^* = 0) = 0 \tag{45}$$

where,

$$\overline{g}^* = \int_{\mu'=-1}^{1} \frac{g \cdot r_0^2 \cdot r^{*\frac{1}{2}}}{k(T_0 - T_{amb})} P_n(\mu') \, \mathrm{d}\mu' \tag{46}$$

The integration pair in r direction is:

$$\overline{V}^* = \sum_{m=1}^{\infty} \frac{1}{N(\lambda_{nm})} J_{n+\frac{1}{2}}(\lambda_{nm} r^*) \widetilde{V}^*(\lambda_{nm}, n, t) \tag{47}$$

$$\widetilde{V}^* = \int_{r^{*'}=0}^{1} r^{*'} J_{n+\frac{1}{2}}(\lambda_{nm} r^{*'}) \overline{V}^*(r^{*'}, n, t) \, \mathrm{d}r^{*'} \tag{48}$$

where $N(\lambda_{nm})$ is the norm of the Bessel function of the first kind of degree $n + \frac{1}{2}$ corresponding to the convection boundary condition at the droplet surface, Eq. (44):

$$\frac{1}{N(\lambda_{nm})} = \frac{2}{J_{n+\frac{1}{2}}^2(\lambda_{nm})} \frac{\lambda_{nm}^2}{(Bi - \frac{1}{2})^2 + \lambda_{nm}^2 - (n + \frac{1}{2})^2} \tag{49}$$

And λ_{nm} is the eigen value of the eigen function in r direction, $J_{n+\frac{1}{2}}(\lambda_{nm} r^*)$, which is determined by Eq. (10) by substituting $J_{n+\frac{1}{2}}(\lambda_{nm} r^*)$ into Eq. (44).

Thus, apply the integration $\times \int_{r^{*'}=0}^{1} r^{*'} J_{n+\frac{1}{2}}(\lambda_{nm} r^{*'}) \, \mathrm{d}r^{*'}$ to Eqs. (42) and (45) to yield:

$$\frac{\mathrm{d}\widetilde{V}^*}{\mathrm{d}t^*} + \lambda_{nm}^2 \widetilde{V}^* = \widetilde{g}^* \Phi^* \tag{50}$$

$$\widetilde{V}^*(\lambda_{nm}, n, t^* = 0) = 0 \tag{51}$$

with

$$\widetilde{g}^* = \int_{r^{*'}=0}^{1} r^{*'} J_{n+\frac{1}{2}}(\lambda_{nm} r^{*'}) \overline{g}^* \, \mathrm{d}r^{*'} \tag{52}$$

Duhamel's theorem is applied to solve Eq. (50) with its initial condition Eq. (51). An auxilliary equation is set as below with same initial condition:

$$\frac{\mathrm{d}X}{\mathrm{d}t^*} + \lambda_{nm}^2 X = \widetilde{g}^* \tag{53}$$

$$X(t^* = 0) = 0 \tag{54}$$

Solve Eqs. (53) with (54) to find:

$$X = \frac{\widetilde{g}^*}{\lambda_{nm}^2} \left(1 - e^{-\lambda_{nm}^2 t^*}\right) \tag{55}$$

And thus the solution for $\widetilde{V}^*$ can be expressed as:

$$\widetilde{V}^* = \int_{\tau^*=0}^{t^*} \frac{\mathrm{d}\Phi^*}{\mathrm{d}t^*} X \, \mathrm{d}\tau^* \tag{56}$$

Finally, the final solution for dimensionless temperature distribution in the droplet is obtained by applying the inverse integral transformations, Eq. (47) and Eq. (39) to Eq. (56) and divided by $r^{*\frac{1}{2}}$ successively:

$$T^* = \sum_{n=0}^{\infty} \sum_{m=1}^{\infty} \frac{P_n(\mu)}{N(n)} \frac{J_{n+\frac{1}{2}}(\lambda_{nm} r^*)}{r^{*\frac{1}{2}} N(\lambda_{nm})} \widetilde{V}^*$$

$$= \sum_{n=0}^{\infty} \sum_{m=1}^{\infty} \frac{P_n(\mu)}{N(n)} \sqrt{\frac{2\lambda_{nm}}{\pi}} \frac{j_n(\lambda_{nm} r^*)}{N(\lambda_{nm})} \widetilde{V}^* \tag{57}$$
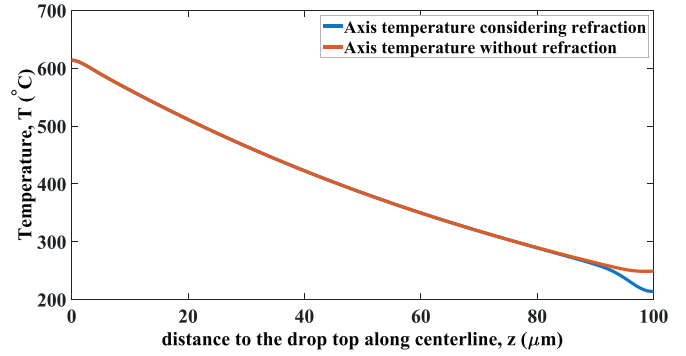

Fig. 11. Temperature distribution along the axis of Ag20 droplet by $I_0 = 13.4 \, \mathrm{GW/cm^2}$ and $t = 1.83 \, \mu s$ with or without considering refraction of the laser in the droplet.
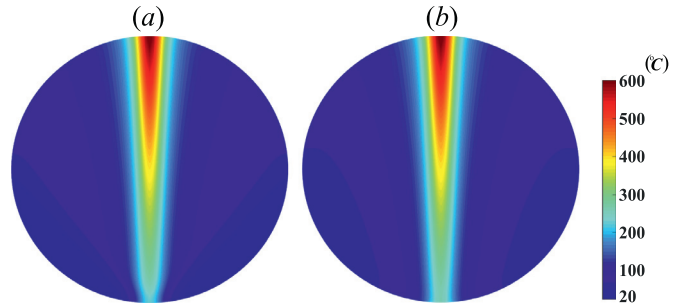

Fig. 12. Temperature distribution for Ag20 droplet with $I_0 = 13.4 \, \mathrm{GW/cm^2}$ and $t = 1.83 \, \mu s$. Ag20 droplet diameter $= 100 \, \mu m$. (*a*) With considering refraction of the laser in the droplet. (*b*) Without considering refraction of the laser in the droplet.

Appendix C. Analytical results with or without refraction

The complex energy generation expression in the droplet, $g(r, \theta)$, can be simplified dramatically as $g_s(r, \theta)$ by not considering the effect of refraction which also reduces the calculation time for temperature distribution. Thus $g_s(r, \theta)$ can be expressed as:

$$g_s(r, \theta) = (1 - R)I_0 \gamma e^{-\gamma r_1} J_0^2(k_r r \sin\theta) \tag{58}$$

where,

$$r_1 = \sqrt{r_0^2 - r^2 \sin^2\theta} - r\cos\theta \tag{59}$$

Temperature distribution along droplet axis in Ag20 droplet for $I_0 = 13.4 \, \mathrm{GW/cm^2}$ at time $t = 1.83 \, \mu s$ with or without considering the refraction of the laser is plotted in Fig. 11 for comparison. It shows a similar temperature distribution at the droplet axis where the explosion occurs since the incidence angle near the droplet axis is small and the effect of refraction is weak.

In fact, the temperature distribution nearby the droplet axis is similar with or without considering the refraction of the laser due to the small incidence angle. It can be shown from temperature distributions in Ag20 droplet for $I_0 = 13.4 \, \mathrm{GW/cm^2}$ at time $t = 1.83 \, \mu s$ with or without considering the refraction of the laser in Fig. 12. However, near the bottom surface of the droplet, model with refraction gives more realistic distribution since the incidence angle in these area are large and effect of refraction plays a role. For the purpose of accuracy, the analytical model with refraction is used in this paper, but if finding out the explosion region is the only concern within a limited time, the temperature distribution without refraction can be a good approximation near the droplet axis.

References

[1] E. Castillo-Orozco, R. Kumar, A. Kar, Laser-induced subwavelength structures by microdroplet superlens, Opt. Express 27 (6) (2019) 8130–8142.

[2] P. Buffat, J.P. Borel, Size effect on the melting temperature of gold particles, Phys. Rev. A 13 (6) (1976) 2287.

[3] E. Castillo-Orozco, R. Kumar, A. Kar, Laser electrospray printing of nanoparticles on flexible and rigid substrates, J. Laser Appl. 31 (2) (2019) 022015.

[4] E. Castillo-Orozco, A. Kar, R. Kumar, Electrospray mode transition of microdroplets with semiconductor nanoparticle suspension, Sci. Rep. 7 (1) (2017) 1–10.

[5] J.H. Choi, K. Ryu, K. Park, S.-J. Moon, Thermal conductivity estimation of inkjet-printed silver nanoparticle ink during continuous wave laser sintering, Int. J. Heat Mass Transf. 85 (2015) 904–909.

[6] S.H. Ko, H. Pan, C.P. Grigoropoulos, C.K. Luscombe, J.M.J. Fréchet, D. Poulikakos, Air stable high resolution organic transistors by selective laser sintering of ink–jet printed metal nanoparticles, Appl. Phys. Lett. 90 (14) (2007) 141103.

[7] H. Wada, T. Mori, High-resolution transparent carbon electrodes for organic field-effect transistors patterned by laser sintering, Appl. Phys. Lett. 95 (25) (2009) 333.

[8] A. Rahaman, A. Kar, X. Yu, Thermal effects of ultrafast laser interaction with polypropylene, Opt. Express 27 (4) (2019) 5764–5783.

[9] T. Wickramasooriya, R. Vaidyanathan, A. Kar, Laser non-uniform heating of moving thin wires below the Biot number criterion of uniform temperature, Lasers Manuf. Mater. Process. 3 (2) (2016) 111–130.

[10] M. Jaunich, S. Raje, K. Kim, K. Mitra, Z. Guo, Bio-heat transfer analysis during short pulse laser irradiation of tissues, Int. J. Heat Mass Transf. 51 (23–24) (2008) 5511–5521.

[11] X. Tian, G. Peng, M. Yan, S. He, R. Yao, Process prediction of selective laser sintering based on heat transfer analysis for polyamide composite powders, Int. J. Heat Mass Transf. 120 (2018) 379–386.

[12] M. Monde, M.N. Hasan, Homogeneous nucleation boiling explosion phenomena under non-equilibrium condition, in: Proc. Int. Conf. on Mechanical Engineering, 2011.

[13] S. Liu, F. Zhang, S. Dong, H. Zhang, F. Liu, Characteristics analysis of droplet transfer in laser-MAG hybrid welding process, Int. J. Heat Mass Transf. 121 (2018) 805–811.

[14] M. Uršič, M. Leskovar, M. Bürger, M. Buck, Hydrodynamic fine fragmentation of partly solidified melt droplets during a vapour explosion, Int. J. Heat Mass Transf. 76 (2014) 90–98.

[15] A. Saha, S. Basu, R. Kumar, Scaling analysis: equivalence of convective and radiative heating of levitated droplet, Appl. Phys. Lett. 100 (20) (2012) 204104.

[16] R. Kumar, E. Tijerino, A. Saha, S. Basu, Structural morphology of acoustically levitated and heated nanosilica droplet, Appl. Phys. Lett. 97 (12) (2010) 123106.

[17] L. Jiao, R. Chen, X. Zhu, Q. Liao, IR laser caused droplet evaporation on the hydrophobic surface, Int. J. Heat Mass Transf. 94 (2016) 180–190.

[18] S. Basu, B.M. Cetegen, Modeling of thermophysical processes in liquid ceramic precursor droplets heated by monochromatic irradiation, J. Heat Transf. 130 (7) (2008).

[19] J.D. Pendleton, Water droplets irradiated by a pulsed CO_2 laser: comparison of computed temperature contours with explosive vaporization patterns, Appl. Opt. 24 (11) (1985) 1631–1637.

[20] B.-S. Park, R.L. Armstrong, Laser droplet heating: fast and slow heating regimes, Appl. Opt. 28 (17) (1989) 3671–3680.

[21] P. Kafalas, A.P. Ferdinand, Fog droplet vaporization and fragmentation by a 10.6-μm laser pulse, Appl. Opt. 12 (1) (1973) 29–33.

[22] M. Shusser, D. Weihs, Explosive boiling of a liquid droplet, Int. J. Multiph. Flow 25 (8) (1999) 1561–1573.

[23] H.K. Park, C.P. Grigoropoulos, C.C. Poon, A.C. Tam, Optical probing of the temperature transients during pulsed-laser induced boiling of liquids, Appl. Phys. Lett. 68 (5) (1996) 596–598.

[24] A. Takamizawa, S. Kajimoto, J. Hobley, K. Hatanaka, K. Ohta, H. Fukumura, Explosive boiling of water after pulsed IR laser heating, Phys. Chem. Chem. Phys. 5 (5) (2003) 888–895.

[25] D.R. Alexander, J.G. Armstrong, Explosive vaporization of aerosol drops under irradiation by a CO 2 laser beam, Appl. Opt. 26 (3) (1987) 533–538.

[26] R.G. Pinnick, A. Biswas, R.L. Armstrong, S.G. Jennings, J.D. Pendleton, G. Fernández, Micron-sized droplets irradiated with a pulsed CO 2 laser: measurement of explosion and breakdown thresholds, Appl. Opt. 29 (7) (1990) 918–925.

[27] B.-S. Park, A. Biswas, R.L. Armstrong, R.G. Pinnick, Delay of explosive vaporization in pulsed laser-heated droplets, Opt. Lett. 15 (4) (1990) 206–208.

[28] T. Josyula, Z. Wang, A. Askounis, D. Orejon, S. Harish, Y. Takata, P.S. Mahapatra, A. Pattamatta, Evaporation kinetics of pure water drops: thermal patterns, Marangoni flow, and interfacial temperature difference, Phys. Rev. E 98 (5) (2018) 052804.

[29] A. Askounis, Y. Kita, M. Kohno, Y. Takata, V. Koutsos, K. Sefiane, Influence of local heating on Marangoni flows and evaporation kinetics of pure water drops, Langmuir 33 (23) (2017) 5666–5674.

[30] D. Li, K. Imasaki, Laser-bessel-beam-driven electron acceleration, Jap. J. Appl. Phys. 44 (8R) (2005) 6079.

[31] D.E. Gray, et al., American Institute of Physics Handbook, McGraw-Hill, 1972.

[32] D.W. Hahn, M.N. Özisik, Heat Conduction, John Wiley & Sons, 2012.

[33] B.E.A. Saleh, M.C. Teich, Fundamentals of Photonics, John Wiley & sons, 2019.

[34] M. Born, E. Wolf, Principles of Optics: Electromagnetic Theory of Propagation, Interference and Diffraction of Light, Elsevier, 2013.